Integrated PV Capacity Firming and Energy Time Shift Battery Energy Storage Management Using Energy-Oriented Optimization

Sherif A. Abdelrazek, *Student Member, IEEE*, and Sukumar Kamalasadan, *Member, IEEE*

***Abstract*—In this paper, we propose a complete active-power-management scheme for the control of battery energy-storage systems (BESSs) for two main applications: 1) photovoltaic (PV) capacity firming and 2) energy time shift (ETS). In the proposed approach, first two control algorithms are designed to provide active-power set points to BESS for the above applications. Then, an optimization routine for integrating these controllers is designed. The proposed approach uses an energy-conservation method to integrate these two applications of energy-storage system. The designed algorithm was tested on a transient simulation platform and then implemented on a 720-node actual power distribution feeder. The main advantage of the proposed method is that the algorithm can be used to optimize multiple functions and perform simultaneous control of BESS.**

***Index Terms*—Batteries, energy storage-management systems (SMSs), energy time shift (ETS), message bus, peak-load shaving, renewable capacity firming.**

NOMENCLATURE

System Topology

BESMS	Battery energy-storage and management system.
SMS	Storage-management system.
BESS	Battery energy-storage system.
BMS	Battery management system.
PWM	Pulsewidth modulation.
PV	Photovoltaic
PVCF	PV capacity firming.
ETS	Energy time shift.
IDA	Intermittency detection algorithm.
IDAOP	IDA output.
AFC	Adaptive filtering control.

Algorithm Parameters

$P_{\text{set}}(t)$	Active-power set point.
$P_{\text{pr}}(t)$	Firming active-power reference.
$P_{\text{Dset}}(t)$	Discharge active-power set point.
$P_{\text{Cset}}(t)$	Charge active-power set point.
$P_{\text{pv}}(t)$	Instantaneous active PV power.
$P_{\text{pv}}^{k}(t)$	Instantaneous active PV power for day k.
$P_{\text{scmp}}(t)$	Instantaneous smoothed characteristic maximum PV power.
R_n	Maximum daily rate of change of active power for PV station.
R_m	Maximum allowed value for weighing factor time differential.
R_m	Maximum allowed rate of change of smoothed characteristic maximum PV curve.
$m_e(t)$	Dynamic BESS energy-oriented firming reference weighing factor.
$P_{\text{pr}}^{\text{de}}(t)$	Instantaneous value of dynamic energy-oriented firming reference.
SoC_T	Target state-of-charge (SoC).
T_T	Target time for target SoC.
T_{est}	Predicted time of feeder peak-load.
R_{sw}	PV power intermittency detection threshold.
E_{Bcap}	Energy capacity of BESS.

Implementation Infrastructure

SGL	Smart grid laboratory.
DNP	Distributed network protocol.
MQTT	Message queue telemetry transport.
DMZ	Demilitarized zone.

Manuscript received June 15, 2015; revised October 16, 2015 and January 5, 2016; accepted January 21, 2016. Date of publication February 18, 2016; date of current version May 18, 2016. Paper 2015-IACC-0381.R2, presented at the 2014 IEEE Industry Applications Society Annual Meeting, Vancouver, BC, Canada, October 5–9, and approved for publication in the IEEE TRANSACTIONS ON INDUSTRY APPLICATIONS by the Industrial Automation and Control Committee of the IEEE Industry Applications Society.

The authors are with the Department of Electrical and Computer Engineering, University of North Carolina at Charlotte, Charlotte, NC 28223 USA (e-mail: sabdelr3@uncc.edu; skamalas@uncc.edu).

Color versions of one or more of the figures in this paper are available online at http://ieeexplore.ieee.org.

Digital Object Identifier 10.1109/TIA.2016.2531639

I. INTRODUCTION

THE applications in which energy storage systems are used hold considerable value to energy producers, grid operators, and, in turn, energy consumers. As concluded in [1], energy storage systems can provide efficient solutions for various issues in modern electrical networks including microgrids. For different applications, different technologies of energy storage can be used. As mentioned in [2], these applications include electric ETS, voltage support, transmission support, time-of-use energy management, demand-change management, renewable ETS, and renewable capacity firming. Upon studying the usability of various energy-storage technologies for various applications, it is found that flywheel energy storage (FES) is suitable for applications that address dynamic stability [4], transient stability [5], voltage support [6], and power quality improvement [7]. Nevertheless, FES cannot present value for area control/frequency regulation or transmission capability improvement [2]. On the other hand, superconducting magnetic

energy storage (SCMES) and BESS are suitable for applications that improve dynamic stability [8], [9], transient stability [10], [11], voltage support [12], area control/frequency regulation [13], [14], transmission capability [13], [14], and power quality [5], [15]. BESS was found to be the most economically viable energy-storage technology for such applications.

Several works has focused on BESS management for application such as PVCF [16]–[21]. Even though there is no unique way to smooth the PV output, [16] and [17] focus on a moving-average-based ramp-rate control. A dynamic filtering controller and dynamic rate-limiter approach are used in [16], and an exponential moving-average method has been utilized in [17] for controlling the battery for PV smoothing applications. However, these works do not consider multiple functions for the storage that can be used simultaneously at a given point of time. In our earlier work [18]–[20], we proposed multiple-function controller architecture for more than one application of BESS.

In this paper, two control algorithms are designed for controlling BESS power and energy; the first one for PV smoothing and the second one for ETS applications. The PV smoothing algorithm controls BESS power to smooth the intermittency of the PV farm (connected to the feeder separately), and the ETS algorithm controls the BESS energy so that the battery is discharged during the peak-load conditions. Then, the SoC of the battery is optimized so that both these algorithms can be run simultaneously on the SMS. To test the performance of the system, first an electromagnetic transient program (EMTP) model of the actual 720 node power-distribution system in the power grid of South Eastern United States is designed. The models are first validated with the real data from the feeder for testing purpose. Using the EMTP-validated model, the performance of the control algorithms is analyzed. Further, the designed controller is used to control the actual 750 kWh BESS connected to the actual distribution grid via a remote control-communication infrastructure, where real measurements (from PV station, BESS, and feeder substation) are streamed to the remote controller, and in turn, active-power charge and discharge set points of the battery are sent back to BESS. The main advantages of the proposed architecture are as follows.

1) The PV smoothing and ETS algorithms are adaptable in nature.
2) The SoC optimization of these algorithms allows for a co-optimization methodology that can be used to simultaneously run these algorithms.
3) The proposed architecture can be implemented in the field.

This paper is organized as follows. In Section II, the system topology is discussed. Section III discusses the proposed control methodology, Section IV describes the practical implementation architecture and results on the actual feeder, and Section V concludes this paper.

II. System Topology

First, to design and test the control algorithms, a real feeder model is designed. The modeling of the feeder, PV farm, and battery is based on a real distribution feeder located in the power grid of South Eastern United States. In this feeder, the battery and SMS are connected to one location, and the PV farm is located separately from the battery. The details of the feeder and the devices are discussed next. The models are prepared for the feeder and each of the field devices, and are validated based on the actual field data.

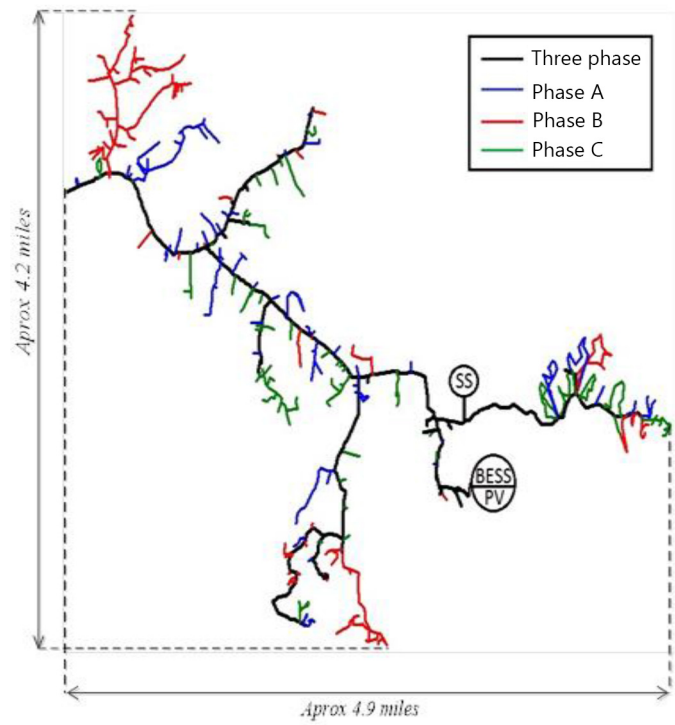

Fig. 1. Practical 720 node distribution feeder with substation and BESS location shown.

A. Distribution Feeder

The distribution feeder shown in Fig. 1 is a practical medium-voltage 12.47 kV residential radial distribution feeder consisting of 720 nodes. Fig. 2 shows the aggregated model of the described distribution feeder used for first analyzing the controller performance. A 1.25-MVA/750-kWh (3 h) BESS is connected in conjunction with a 1-MW PV station at the point of common coupling (PCC) shown in both figures. As shown, the PCC is practically located at the near-end of the distribution feeder. Feeder load is modeled utilizing three aggregated spot loads across the feeder. The circuit impedances shown are aggregations of total feeder impedances across the practical feeder. These impedance values are calculated using practical feeder data.

B. Battery Energy Storage and Management System

As shown in Fig. 3, the BESMS model consists of a lithium polymer battery model, which was developed and validated with methods similar to that in [22]. The SMS topology studied is constructed to allow operation in the four PQ power quadrants. In other words, reactive power supply and consumption

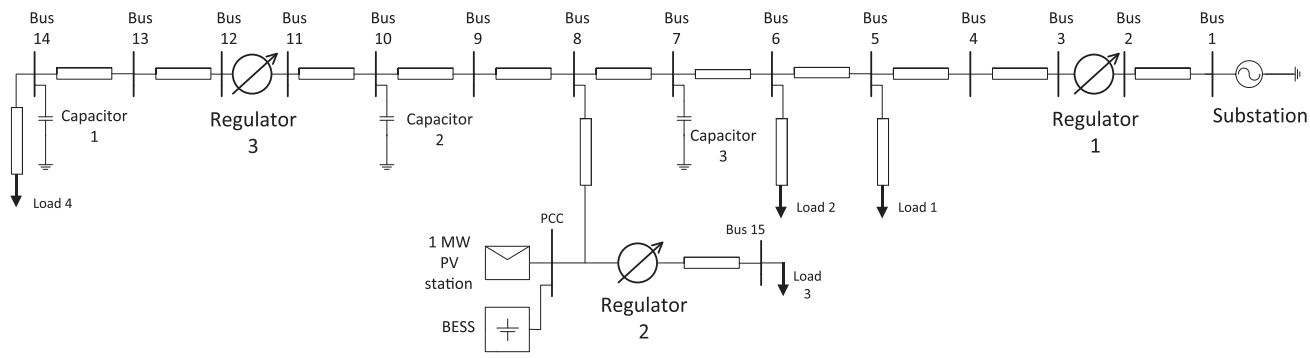

Fig. 2. Sixteen bus aggregated feeder model.

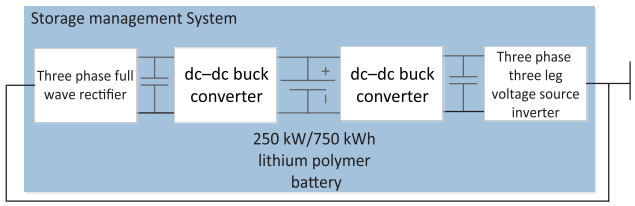

Fig. 3. Topology of studied SMS.

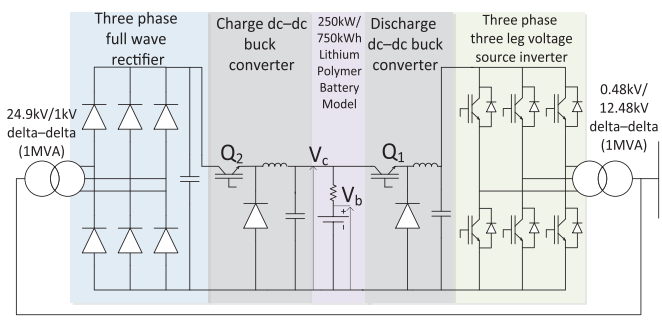

Fig. 4. SMS EMTP simulation model.

are possible during both charge and discharge states of the battery. This would not be achievable with a bidirectional inverter. The topology shown in Fig. 4 includes (in its discharge path) the battery model connected to a dc–dc buck converter. The buck converter is connected to a three-phase three-leg voltage source inverter, which has a built-in filter for harmonic suppression and reactive power support.

The SMS charge path includes a three-phase full-wave rectifier connected (on its ac side) to the PCC through delta-delta transformer. The dc side of the rectifier is connected to buck converter.

1) Discharge Path: During battery discharge cycle, switch (Q_1) shown in Fig. 4 is controlled to hold the dc-link voltage to a set value. Switch (Q_2) remains open during discharge operation. Inverter switches are controlled by pulse PWM. Modulation index is set according to the reactive power required to be supplied or consumed from the feeder ($Q_{\text{set}}(t)$). The phase of the PWM reference signal controls the active-power output and is set by the positive values of the active-power reference signal ($P_{\text{set}}(t)$).

2) Charge Path: During the charge cycle, power is provided to the battery through the three-phase full-wave rectifier

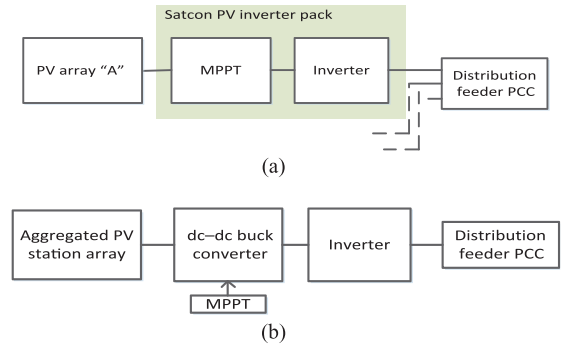

Fig. 5. PV station. (a) Practical system. (b) Modeled system.

and the second buck converter. The rectifier sets the voltage at the charge dc link. Switch (Q_2) shown in Fig. 4 is controlled to buck the rectified voltage at the dc link to the required output voltage value for the required battery-charge rate. The voltage (V_c) required to charge the battery is calculated from the desired charge rate, which is represented by negative values of the active-power reference signal ($P_{\text{set}}(t)$).

C. PV Station

The PV station described is connected on the same bus as that of the BESS. As shown in Fig. 5(a), the practical system consists of six separate arrays connected to six separate inverters, which are commonly connected to the PCC. Each array utilizes different PV architecture. Nevertheless, 70% of the total PV station capacity is of the same module (Yingli) and inverter-type (Satcon). Thus, for evaluation purpose, the system is aggregated into a single array with a single inverter as shown in Fig. 5(b).

D. Model Validation

The PV module and inverter used for the aggregated PV station array are such that the model is the most commonly used in the practical PV farms. After the models are developed in EMTP domain, validation is performed. For example, the irradiance profile obtained from the field sensor for certain days is used as an input data, and the PV output from the EMTP PV farm model is compared with the PV farm output from the field. Similar methods of input-/output-data-based validations

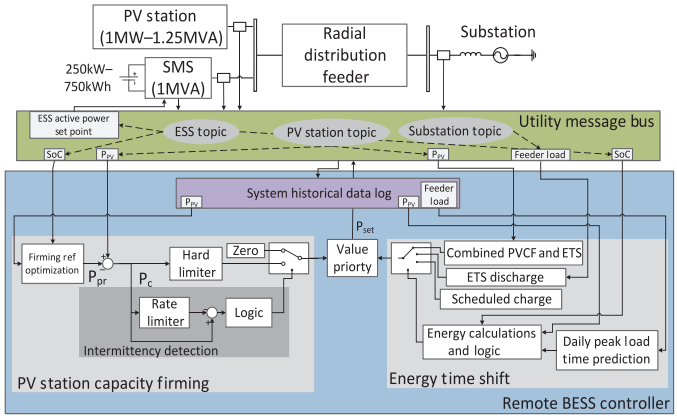

Fig. 6. Block diagram schematic for PV station capacity firming algorithm.

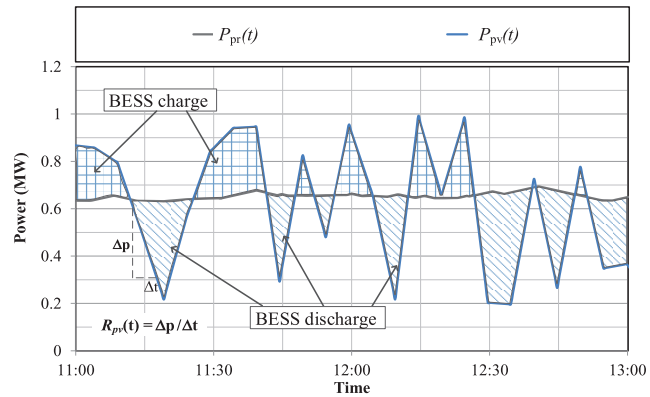

Fig. 7. BESS response to output PV power and reference power values.

are performed for other devices such as BESS and SMS. Due to space limitation, the details are excluded.

III. Proposed BESS Control Methodology

The proposed control methodology relies on gathering data streams from different points of the described distribution feeder. These data sets are published to a field message bus, where data can be accessed by authorized system operators. A remote dedicated system which is used to subscribe to the field message bus and acquire data inputs needed for the BESS applications is implemented. The proposed BESS controller is situated at a remotely located laboratory, where real-time system data are streamed through the utility-operated field message bus as shown in Fig. 6. Both real-time system data and recorded historical data are used to calculate the required BESS active-power reference ($P_{\text{set}}(t)$) and identify optimal firming degree.

A. PVCF Algorithm

The BESS control algorithm for PVCF aims to minimize PV station power-swings. The described PVCF algorithm targets large power-swings occurring at noon when PV output is at its peak. These swings are the most crucial to minimize transients in the feeder. A PV reference value is used to determine the optimal corrected PV power output (PCC power) during power-swings. This reference curve is deduced taking into account the PV station characteristics, BESS size, and real-time SoC. The PVCF algorithm depends on a four-stage AFC methodology. First, a characteristic PV curve is developed based on daily PV power output recorded from historical data. Second, a smooth characteristic PV curve is developed. Third, a firming power reference is developed that considers real-time PV station power-swing magnitudes, battery capacity, and targeted SoC at the end of the firming period. Fourth, an IDA triggers the BESS to commence and halt firming based on PV station output ramp rate. The details of the algorithms are discussed next.

1) Characteristic PV Curve Calculation: The PV reference power algorithm utilizes short-term historical PV station output to develop a characteristic maximum PV curve for the PV station location at that time of the year. This curve is used to ultimately deduce an optimal power reference, which is compared with instantaneous PV output power to determine the manner in which the BESS active power should be dispatched to attain firmed PCC power. As shown in (1) and an example in Fig. 7, the instantaneous value of the BESS active-power reference signal $[P_{\text{set}}(t)]$ for PVCF is equal to the difference between the power reference and the real-time output power of the PV station

$$P_{\text{set}}(t) = P_{\text{pr}}(t) - P_{\text{pv}}(t). \tag{1}$$

For a daily-output power of PV station $P_k(t)$, where k signifies the day number; $k = 1, 2, 3, 4, \ldots, n$, the characteristic maximum and minimum PV curve is given by

$$P_m^{\max}(t) = \max\left\{P_{\text{pv}}(t), P_{\text{pv}}(t-\Delta t), \ldots, P_{\text{pv}}(t-(n-1)\Delta t)\right\} \tag{2}$$

$$P_m^{\min}(t) = \min\left\{P_{\text{pv}}(t), P_{\text{pv}}(t-\Delta t), \ldots, P_{\text{pv}}(t-(n-1)\Delta t)\right. \tag{3}$$

where $T = n\Delta t$ and n represents the number of previous days utilized to form the characteristic maximum and minimum PV curves. Then, the reference power can be written as

$$P_m(t) = \frac{\sum_{k=1}^{n} \mu_k P_m^{\max}(t) - \sum_{k=1}^{n} \mu_k P_m^{\min}}{\sum_{k=1}^{n} \mu_k}. \tag{4}$$

For a daily input data and to capture maximum power from the PV farm, the daily reference curve can be represented as

$$P_m(t) = \max\left\{P_m(t), P_m(t-\Delta t), \ldots, P_m(t-(n-1)\Delta t)\right\} \tag{5}$$

where t represents current day and Δt represents the previous days or in a general form

$$P_m(t) = \max\left(P_1(t), P_2(t), P_3(t), \ldots, P_n(t)\right). \tag{6}$$

Considering the above, the rate of power changes can be represented as

$$rP_m(t) = \frac{\Delta P_m(t)}{\Delta t} = \frac{P_m(t) - P_m(t-\Delta t)}{\Delta t}. \tag{7}$$

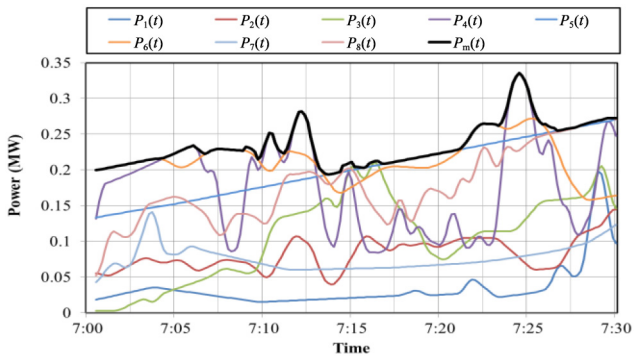

Fig. 8. Characteristic maximum PV curve.

It could be noted that (7) can be written as a function of maximum and minimum power from the PV as

$$rP_m(t) = f_{\text{PV}}\left(\frac{P_m{}^{\max}(t) - P_m{}^{\min}(t)}{P_m(t)}\right). \tag{8}$$

Let U_l be the maximum-allowed ramp rate and L_l be the minimum-allowed ramp rate, then by the same token

$$U_l(t) = \frac{P_m{}^{\max}(t) - P_m{}^{\max}(t-\Delta t)}{\Delta t} \tag{9}$$

and

$$L_l(t) = \frac{P_m{}^{\min}(t) - P_m{}^{\min}(t-\Delta t)}{\Delta t}. \tag{10}$$

An example characteristic maximum curve is shown in Fig. 8.

2) Smoothed Characteristic Maximum Curve Calculation: The smoothed characteristic maximum power curve (SCMP) is defined as

$$P_{\text{scmp}}(t) = \text{a}P_m(t) + b(P_{\text{scmp}}(t-\Delta t) + R_m\Delta t) + c\,(P_{\text{scmp}}(t-\Delta t) + R_m\Delta t) \tag{11}$$

where a, b, and c are digits of a 3-bit binary number (Ψ), a being the most significant bit, and c the least significant. Let us define λ as

$$\lambda(t) = \frac{P_m(t) - P_{\text{scmp}}(t-\Delta t)}{\Delta t} \tag{12}$$

$$\Psi(t) = \begin{cases} 100, & \text{for } -R_m < \lambda(t) < R_m \\ 010, & \text{for } \lambda(t) > R_m \\ 001, & \text{for } \lambda(t) < -R_m \end{cases} \tag{13}$$

where R_m is defined as the maximum-allowed rate of change of the smoothed characteristic maximum PV power with respect to time. R_m is directly related to R_n, which is defined here as the PV station's nominal characteristic rate of change of output active power. In other words, it can be described as the maximum rate of change of a PV station's output power with respect to time, in the absence of clouds and any rapid power-swings. The value of R_n is directly related to the size of the PV station in question. Assuming a 1-MW PV station, $P_m(t)$ is regressed

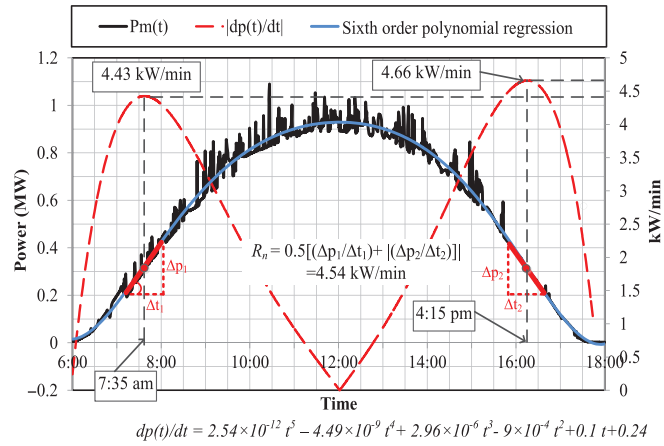

Fig. 9. 1-MW PV station sixth-order polynomial rate of change and maximum ramp rate identification.

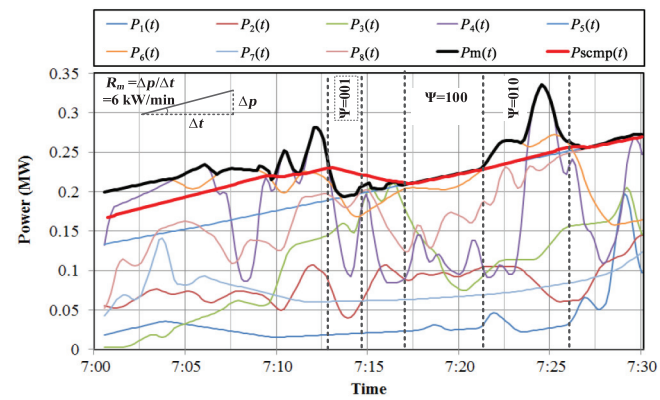

Fig. 10. Smoothed characteristic maximum PV power.

to attain the sixth-order polynomial as shown below

$$p(t) = 4.24 \times 10^{-13}\, t^6 - 8.98 \times 10^{-10}\, t^5 + 7.4 \times 10^{-7}\, t^4 - 3 \times 10^{-4}\, t^3 + 0.05\, t^2 + 0.24\, t + 15.31. \tag{14}$$

The attained polynomial is differentiated with respect to time to attain $(dp(t)/dt)$ as shown in Fig. 9. Since irradiance is approximately symmetrical across noon, single R_n and R_m values are defined for both increasing and decaying PV power output. Therefore, the maximum positive and negative rates of changes of the regressed sixth-order polynomial are averaged to deduce R_n for a 1-MW station. The value of R_m is chosen to be 130% of R_n to allow for curve settling after fluctuations of $P_m(t)$. Fig. 10 shows $P_{scmp}(t)$ after utilizing an R_m value of 6 kW/min.

3) Firming Reference Calculation: Here, a firming reference power considering the ramp rates and the battery state of charge is designed. The firming reference $[P_{\text{pr}}(t)]$ is a fraction of the SCMP curve. This can be written as

$$P_{\text{pr}}(t) = m(t) \times P_{\text{scmp}}(t). \tag{15}$$

The firming reference value determines the degree of attainable firming. During PV power-swings, it dictates the extent to which the BESS intervenes. Since, varying the weighting factor

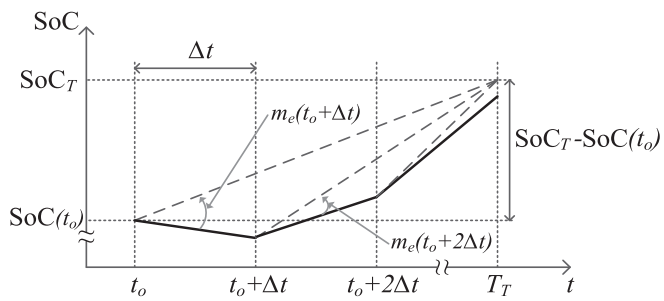

Fig. 11. m_e calculation for energy-oriented firming reference power.

$m(t)$ can be used to control the degree of firming and, in turn, the battery state-of-charge (SoC) throughout the firming period, its value is used to maximize the SoC at the time of predicted feeder peak-load and also maintain sufficient firming. This can be accomplished as follows. For a certain time step (Δt)

$$\Delta \text{SoC} \times E_{\text{cap}} = \left(P_{\text{pv}}(t) - m_e(t) P_{\text{scmp}}(t)\right) \Delta t \tag{16}$$

where E_{Bcap} is the battery energy capacity and Δ SoC is the change in SoC. The weighting factor $m_e(t)$ is defined as

$$m_e\left(t+\Delta t\right) = \frac{P_{\text{pv}}(t)}{P_{\text{scmp}}(t)} - \frac{E_{\text{cap}}}{P_{\text{scmp}}(t)} \frac{\Delta \text{SoC}}{\Delta t} : \left|\frac{dm_e(t)}{dt}\right| < r_m \tag{17}$$

$$\frac{\Delta \text{SoC}}{\Delta t} = \frac{\text{SoC}_T - \text{SoC}(t)}{T_T - t} \tag{18}$$

$$P_{\text{pr}}(t) = m_e(t) \times P_{\text{scmp}}(t) : \left|\frac{dP_{\text{pr}}^{\text{de}}(t)}{dt}\right| < R_m. \tag{19}$$

As shown in (17), the value of $m_e(t)$ can be adjusted for each time step (Δt) to allow battery SoC to reach a target value (SoC_T) at a target time (T_T). The manner in which the SoC approaches its target value is shown in Fig. 11. Not reaching the targeted SoC compromises the execution of further energy-storage functions after PVCF. The weighing factor ramp limiter (r_{m}) is then tuned to assess favorability of maximized firming against reaching SoC target.

Further, reaching the targeted SoC before the targeted time compromises firming performance. For this case, target value is 95% SoC at a target time (T_{est}). Considering the typical partially cloudy PV day shown in Fig. 12, the weighing factor $m_e(t)$ varies according to (17) to firm power intermittencies and simultaneously maximize BESS SoC at the end of the day. In turn, the firming reference varies which causes the BESS firming region to shift. The BESS firming region is defined as the region in which the BESS (in light of its capacity) is capable of firming any PV power-swings.

The increase of the BESS SoC from 15% to 80% is apparent in Fig. 13. Also, the firming region attained covers most of the PV power-swings. This implies that, even with the stochastic nature of PV power-swings, efficient performance of PVCF is possible while setting battery SoC to a desired value.

4) Intermittency Detection: Intermittency detection allows idling of the BESS during times when the PV output power is naturally firmed and does not require conditioning. The IDA contributes to conservation of battery life and decreases value

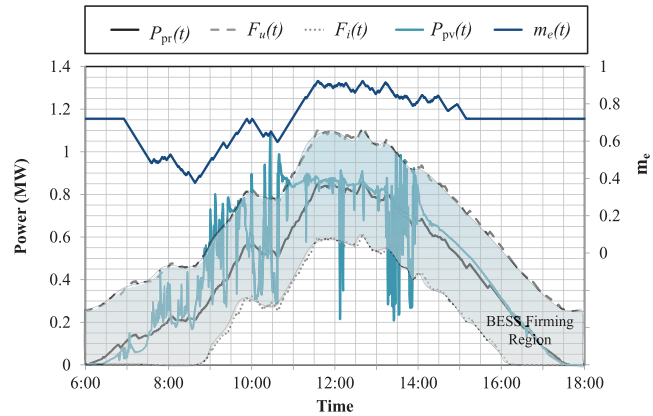

Fig. 12. Firming reference variation with weighing factor.

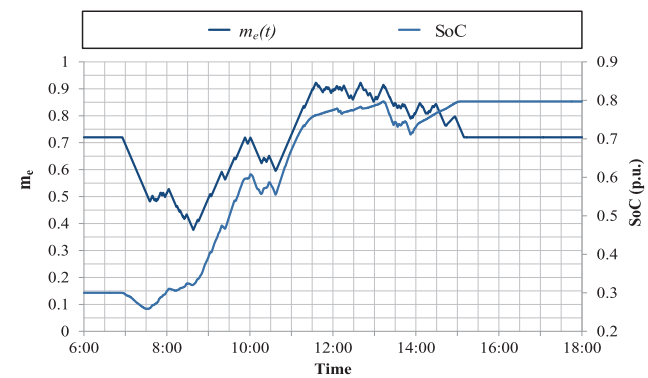

Fig. 13. Weighing factor $m_e(t)$ and SoC variation for partially cloudy PV day.

degradation. The IDA relies on constantly tracking the rate of change of the difference $P_c(t)$ between the output PV power and the PV power reference $[P_{\text{pr}}(t)]$. $P_{cf}(t)$ is equal to $P_c(t)$, such that the first derivative with respect to time of $P_c(t)$ is limited to a certain value (R_{sw}). Equation (21) defines this relation. $P_{cf}(t)$ is then subtracted from $[P_c(t)]$ to obtain (D). If the value of D violates a certain threshold, PV power-swings are identified and firming is commenced. Firming continues till value of D is maintained within limits for a period T_d

$$P_c(t) = P_{\text{pv}}(t) - P_{\text{pr}}(t) \tag{20}$$

$$P_{\text{cf}}(t) = \begin{cases} P_c(t), & \text{for} -R_{\text{sw}} < \frac{P_c(t)-P_{cf}(t-\Delta t)}{\Delta t} < R_{\text{sw}} \\ R_{\text{sw}}\Delta t + P_{cf}\left(t-\Delta t\right), & \text{for } \frac{P_c(t)-P_{cf}(t-\Delta t)}{\Delta t} > R_{\text{sw}} \\ R_{\text{sw}}\Delta t + P_{cf}\left(t-\Delta t\right), & \text{for } \frac{P_c(t)-P_{cf}(t-\Delta t)}{\Delta t} < -R_{\text{sw}} \end{cases} \tag{21}$$

$$D(t) = P_c(t) - P_{\text{cf}}(t). \tag{22}$$

An important trait of the discussed IDA is the application of dual triggers to prevent premature setting of the IDAOP, which would cause unwanted BESS operation. The first threshold violation of $D(t)$ is ignored and used only to set the value of an SR flip-flop that, in turn, sets the IDAOP, provided that a secondary SR flip-flop is also set by a secondary threshold violation of $D(t)$. Fig. 14 shows the operation of the IDA for a sample day. It can be noticed that the algorithm is triggered only during

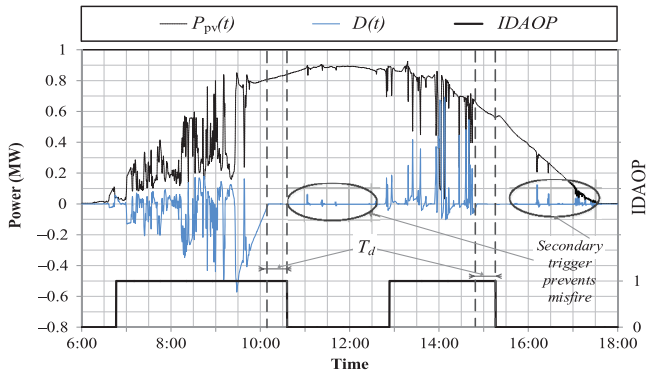

Fig. 14. IDA operation for typical PV station output.

the times of intermittent PV station output or, in other words, during high-scale power-swings. It is also clear that the algorithm output is rested after the PV station output maintains a nonintermittent output state for the specified time period T_d.

B. Energy Time Shift

The ETS algorithm designed hereafter aims to achieve the electricity market equivalent of financial arbitrage, a term widely used by utilities and storage-system operators for ETS applications. The financial definition of arbitrage is the simultaneous purchase and sale of identical commodities across two or more markets to benefit from a discrepancy in their price relationship. In order to efficiently achieve this, the precise prediction of peak-load magnitude and time is crucial. Studying the long time-interval load curves, it was found that applying a moving-average prediction scheme with variable intervals provides accurate prediction. Relying on this, the algorithm checks the battery SoC and calculates the time of day to commence battery discharge, such that the predicted load-curve maximum time lies in the middle of the discharge time period

$$P_{\text{est}}(n+1) = \frac{\sum_{k=n-M+1}^{n} P_k(t)}{M} \tag{23}$$

where n represents the current day and M is the moving-average interval

$$T_{\text{est}}(n+1) = \frac{\sum_{k=n-M+1}^{n} T_k(t)}{M}. \tag{24}$$

$P_k(t)$ and $T_k(t)$ are the magnitude and time of daily peak-loads for the kth day, respectively,

$$T_{\text{Dstart}} = T_{\text{Lpeak}} - \frac{(\text{SoC}) \times E_{\text{Cap}}}{2 \times P_D}. \tag{25}$$

Given a sample of 60-day load-curve data, daily peak-load magnitudes and times are determined and shown in Figs. 15 and 16. Equations (23) and (24) are applied with an arbitrary moving-average interval $M = 5$. The error between actual and predicted peak-load values for varying the moving average period from $M = 1$ to $M = 60$ is shown in Fig. 17. It can be seen that utilizing a moving-average interval less than 10 for peak-load magnitude prediction offers less than 10%

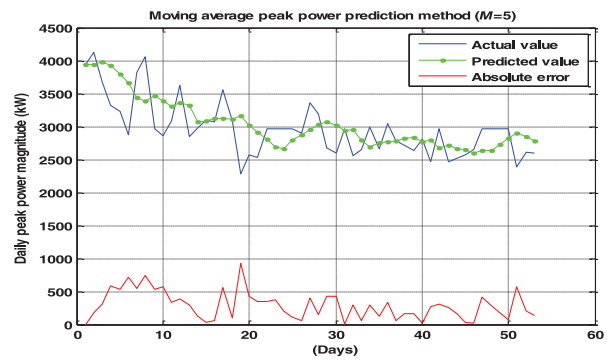

(a)

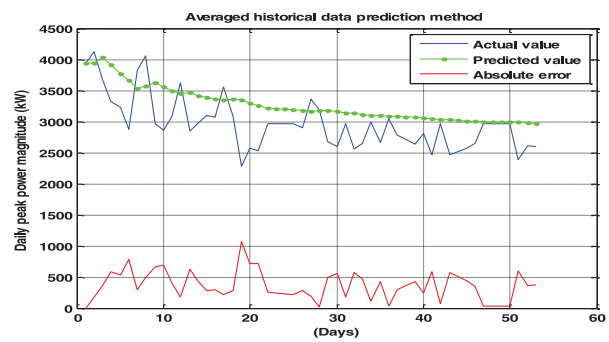

(b)

Fig. 15. (a) Daily peak-load magnitude-prediction using moving-average method. (b) Daily peak-load magnitude-prediction using historical data prediction method (using forecasting).

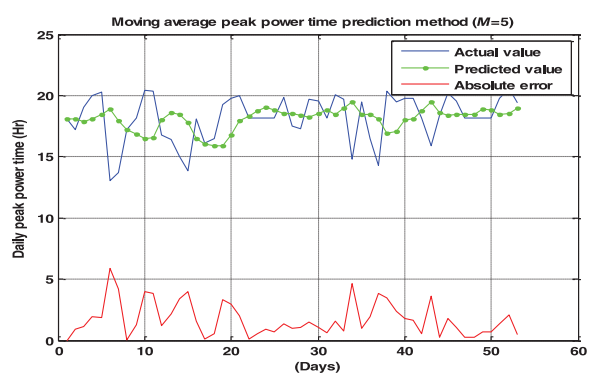

Fig. 16. Daily peak-load time-prediction using moving-average method.

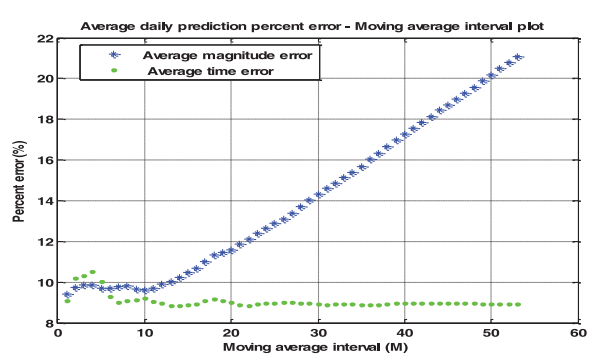

Fig. 17. Moving-average prediction method percent errors.

error, whereas utilizing a moving-average interval greater than 6 for peak-load time prediction offers an error less than 7%. Assuming the battery is fully charged and will perform ETS at maximum battery capacity (250 kW), the total time of discharge

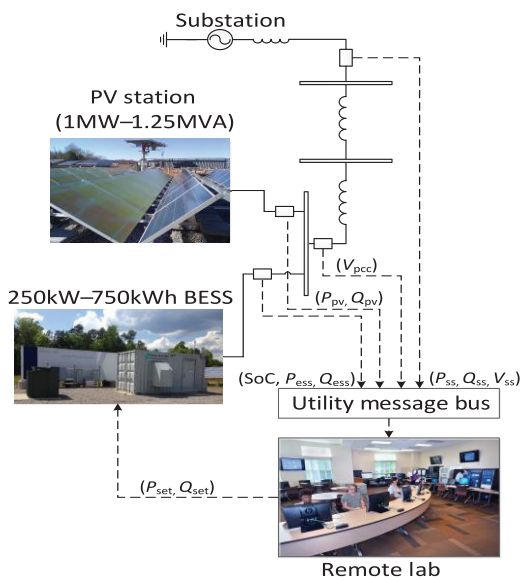

Fig. 18. Communication infrastructure from remote laboratory to battery site.

is 3 h. This covers the average prediction error calculated. Also, since load curves of most days show minimal load at 4:30 A.M., the ETS algorithm is set to start charging the battery at 3 A.M. to avoid the local maximum that occurs at 7:00 A.M. Figs. 12–17 indicate the performance of the proposed algorithm based on the simulations performed using the models developed in EMTP simulator and the controller developed in MATLAB.

C. Combined PVCF and ETS Operation

Utilizing calculated parameters and equations of both applications discussed, a practical and efficient operation of the BESS can be achieved while satisfying desired value of both PVCF and ETS. The predicted time of feeder peak load can be used in the PVCF algorithm to modify the weighting factor m_e using an optimization algorithm. The value of SoC_T and T_T in (18) can be set to maximum BESS SoC and T_{est}, respectively. So, the BESS will perform PVCF while modifying BESS SoC till the time of predicted feeder peak load at which ETS will commence discharge according to T_{Dstart} in (25). These modifications will allow having BESS SoC optimal, so that both applications can be performed.

IV. Real Feeder Implementation Architecture and Results

In order to ensure that the data flow from battery site to the remote laboratory is adequately secure and can be reliably accessed, the network model between the utility's substation local area network and the university network must be considered. Fig. 18 shows the path the data must traverse to be delivered from battery site to the described remote laboratory.

System measurements being streamed through the utility message bus include voltages and active and reactive powers from the BESS, PV station and substation. Further, BESS SoC as well as equipment alarms are also being streamed to ensure system operational safety. Furthermore, the real-time PCC power $[P_{\text{pcc}}(t)]$ and feeder load $[P_{\text{Fload}}(t)]$ is evaluated through the following equations:

$$P_{\text{pcc}}(t) = P_{\text{pv}}(t) + P_{\text{BESS}}(t) \tag{26}$$

$$P_{\text{Fload}}(t) = P_{ss}(t) + P_{\text{pcc}}(t) \tag{27}$$

where $P_{\text{ss}}(t)$, $P_{\text{pv}}(t)$, and $P_{\text{BESS}}(t)$ are the real-time values of substation power output, PV station, and BESS power (positive for discharge and negative for charge), respectively. Since there are no other generating units within the described feeder, (26) becomes valid for feeder load evolution.

A. Communication Infrastructure

Data originates from multiple different devices at the BESS site. These include inverters, reclosers, voltage regulators, and revenue meters. These devices are all connected to a local area network at the substation utilizing the DNP3 protocol. The application that translates the utility standard protocols such as DNP3 or Modbus to MQTT is referred to as a protocol adapter. The data received must traverse the public internet before finally passing the university firewall to the remote laboratory location.

B. Implementation Results

The implementation results for combined PVCF and ETS are presented hereafter for three summer days. The practical operation of the devised algorithm is presented by showing three main figures. The first figure shows firming reference real-time variation and associated parameters, namely, SoC and PV power output. The second figure presents a firming index proposed to quantify the degree of firming performed is presented. Finally, the feeder load compared to the substation generation is presented to signify the effect of the ETS application in shaving feeder peak load. The percentage reduction in feeder peak load is calculated and shown within the figures itself.

Figs. 19–21 represent in their first plot the active PV power output for July 27, July 29, and August 5, respectively. Algorithm active-power output set points $[P_{\text{set}}(t)]$ as well as actual BESS output are shown in the second plot of each figure. The third plot illustrates the corresponding SoC variation. As presented in these figures, online calculation of $P_{\text{pr}}(t)$ is governed by the current state of charge, the time of predicted maximum feeder load, and the PV power output to $P_{\text{scmp}}(t)$ ratio. Equations (17)–(19) express the step changes in $P_{\text{pr}}(t)$.

In an effort to quantify our algorithm's PVCF efficiency, a similar firming index to that applied in [23] is shown in Figs. 22–24. This firming index is defined as the slope of the least-square line of the PCC power 5-min differential plotted against that of the PV power. In other words, e.g., each point on the plot shown in Fig. 22 has an x-axis value equal to the PV power differential over 5 min and a y-axis value equal to the PCC power differential over the same period. So, a point at (400, 60) implies that a 5-min power-swing of 400 kW out of the PV station was reduced to 60 kW at the PCC, after BESS PVCF algorithm intervention. Now, taking the least-square linear regression line's slope over the entire firming period gives

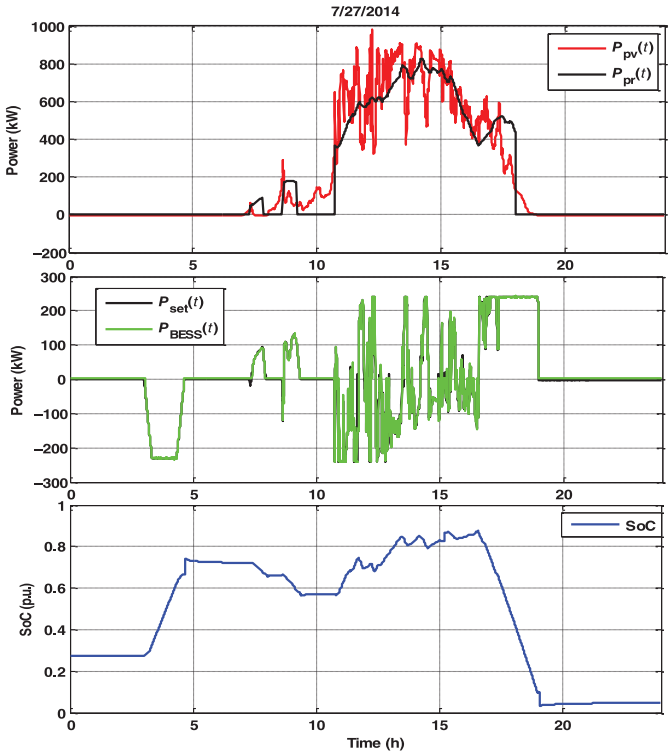

Fig. 19. PV power compared to reference power, algorithm set point compared to actual BESS dispatched power and SoC, respectively, for July 27, 2014, PVCF and ETS.

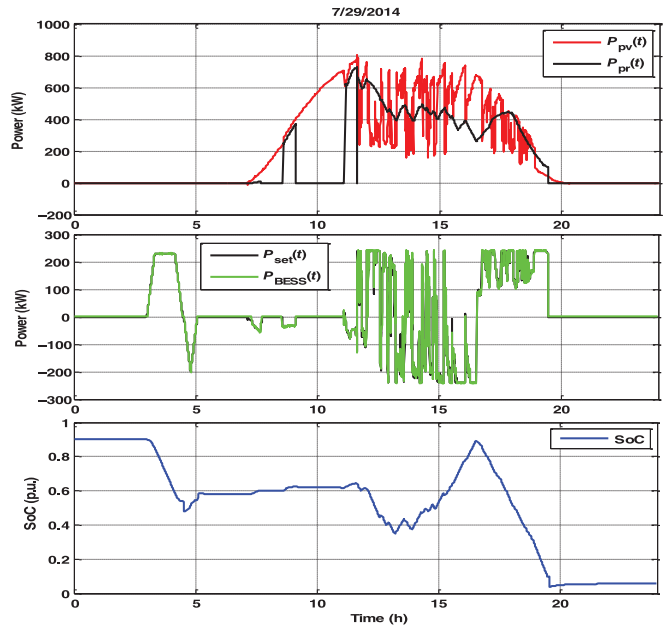

Fig. 20. PV power compared to reference power, algorithm set point compared to BESS dispatched power and SoC, respectively, for July 29, 2014, PVCF and ETS.

an indication of how much firming was performed. Therefore, a unity slope implies no firming. On the other hand, a zero slope implies theoretical maximum firming.

Figs. 25–27 depict the operation of the ETS application. At 3 A.M., the BESS SoC is sought to be adjusted to a suitable value for the PVCF application commencement. Since the BESS is now performing multiple functions, it is no longer required for BESS SoC to be maximized at the beginning of the day in anticipation of ETS discharge. It is rather adjusted to a prechosen value to allow efficient firming. It is worth mentioning that if

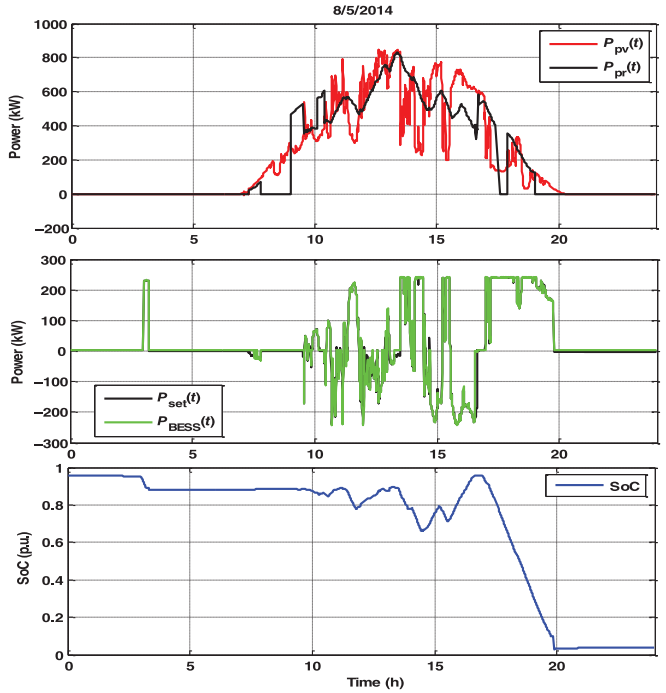

Fig. 21. PV power compared to reference power, algorithm set point compared to BESS-dispatched power and SoC, respectively, for August 5, 2014, PVCF and ETS.

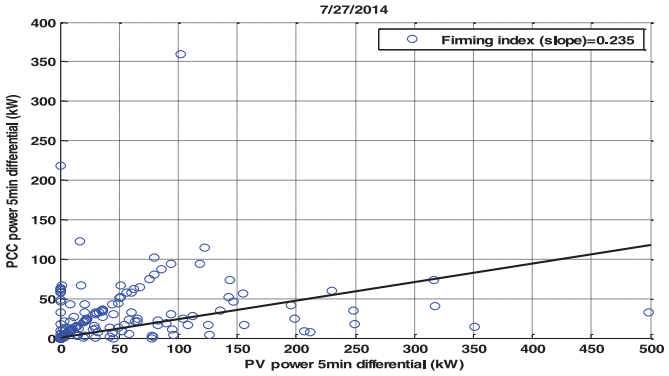

Fig. 22. Firming index for July 27, 2014, PVCF.

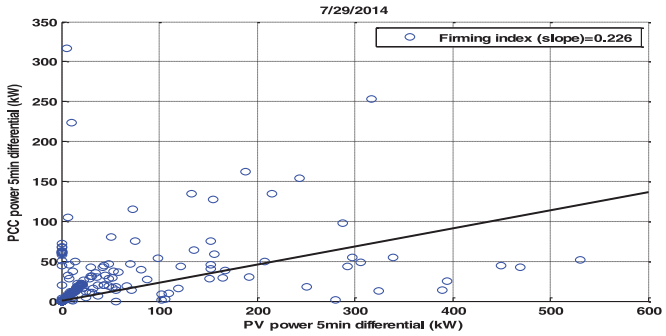

Fig. 23. Firming index for July 29, 2014, PVCF.

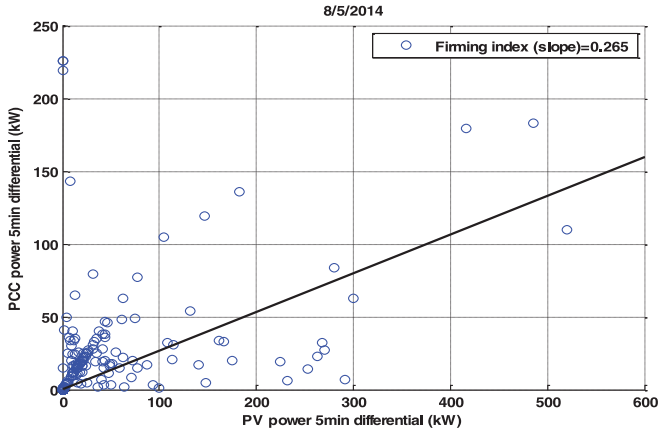

Fig. 24. Firming index for August 5, 2014, PVCF.

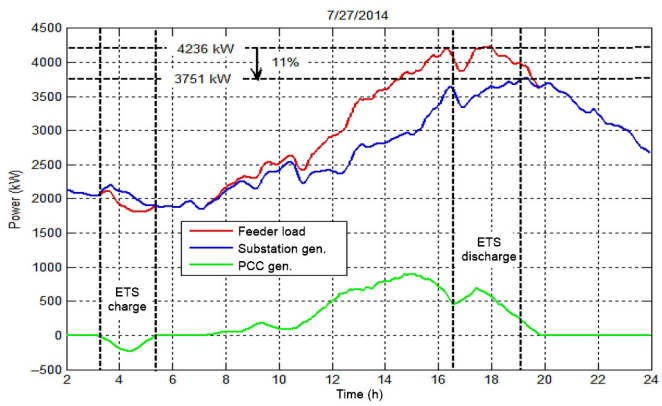

Fig. 25. ETS application shown in the feeder active-power load compared to substation generation for July 27, 2014.

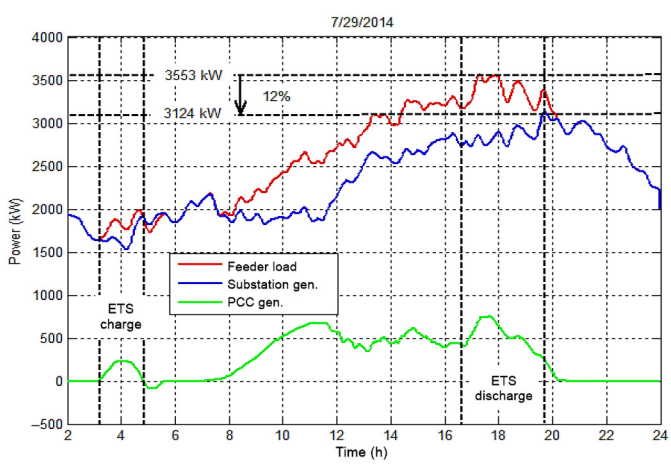

Fig. 26. ETS application results shown in feeder active-power load compared to substation generation for July 29, 2014.

BESS SoC is 100% at that time, PVCF can be performed with only the discharge capabilities of the battery, thus diminishing 50% of the BESS's firming capability. The 3 A.M. time is chosen, since feeder load is usually at its minimum during that time.

ETS charge and ETS discharge represent when the ETS operation is performed. For example, during ETS discharge, the battery discharges. However, during ETS charge, battery optimizes the SoC operation for that day (that may be due to

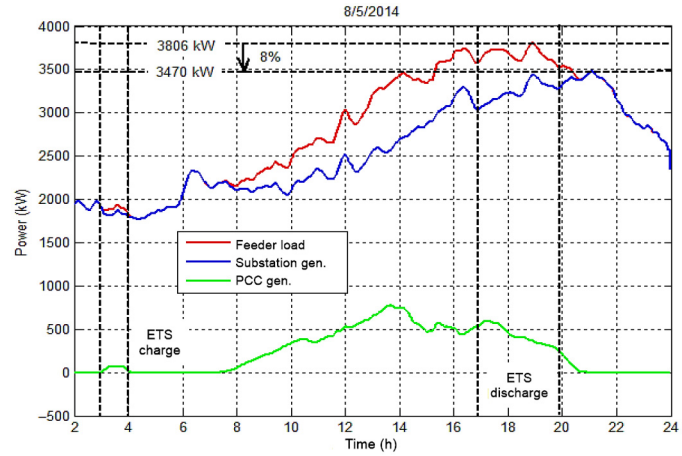

Fig. 27. ETS application results shown in feeder active-power load compared to substation generation for August 5, 2014.

charging or discharging the battery), so that both PVCP and ETS application can be simultaneously performed.

As the day progresses and PVCF is performed, the BESS switches from running the PVCF to ETS as soon as the predicted time-feeder peak load is calculated. During that time, as shown, the substation generation is clearly displaced from feeder load by the combined BESS and PV stations' power generated at the PCC during ETS. The percentages shown on each plot depict the percentage reduction in feeder peak load after BESS ETS application intervention. However, the maximum BESS contribution to peak-load reduction cannot exceed 250 kW. The rest of the power offset is offered by the PV station. Further, during ETS discharge, battery power is dispatched in a manner to induce discharge firming. This allows the battery to perform peak-load shaving and simultaneously perform partial firming.

V. Conclusion

The implementation results displayed led us to conclude that the devised PVCF and ETS applications were successful in performing their respective functions. Optimized PV firming was successful in allowing the opportunity for multiple-function implementations while still performing efficient firming. The ETS feeder peak-load time-prediction method presented valuable peak-load shaving results. The applied communication infrastructure was successful in conveying controller inputs and outputs to and from the BESMS which allowed efficient control. It also provided a great environment for extended testing of the devised algorithms.

References

[1] J. Eyer, "Energy storage for the electricity grid: Benefits and market potential assessment guide, a study for the DOE energy storage systems program," Sandia National Lab, Rep. SAND2010-0815, Feb. 2010.

[2] P. F. Ribeiro, B. K. Johnson, M. L. Crow, A. Arsoy, and Y. Liu, "Energy storage systems for advanced power applications," *Proc. IEEE*, vol. 89, no. 12, pp. 1744–1756, Dec. 2001, doi: 10.1109/5.975900.

[3] S. Teleke, M. E. Baran, A. Q. Huang, S. Bhattacharya, and L. Anderson, "Control strategies for battery energy storage for wind farm dispatching," *IEEE Trans. Energy Convers.*, vol. 24, no. 3, pp. 725–732, Sep. 2009, doi: 10.1109/tec.2009.2016000.

[4] V. Karasik, K. Dixon, C. Weber, B. Batchelder, G. Campbell, and P. Ribeiro, "SMES for power utility applications: A review of technical and cost considerations," *IEEE Trans. Appl. Supercond.*, vol. 9, no. 2, pp. 541–546, Jun. 1999, doi: 10.1109/77.783354.

[5] D. Lieurance, F. Kimball, C. Rix, and C. Luongo, "Design and cost studies for small scale superconducting magnetic energy storage (SMES) systems," *IEEE Trans. Appl. Supercond.*, vol. 5, no. 2, pp. 350–353, Jun. 1995, doi: 10.1109/77.402561.

[6] J. McDowall, "Conventional battery technologies-present and future," in *Proc. IEEE PES Gener. Meeting*, Jul. 27–31, 2010, pp. 1538–1540.

[7] W. V. Hassenzahl, *Capacitors for Electric Utility Energy Storage*, Electric Electric Power Research Institute, Rep. WO 8812, 1997.

[8] R. Boom and H. Peterson, "Superconductive energy storage for power systems," *IEEE Trans. Magn.*, vol. M-8, no. 3, pp. 701–703, Sep. 1972, doi: 10.1109/TMAG.1972.1067425.

[9] R. F. Giese, "Progress toward high temperature superconducting magnetic energy storage (SMES) systems–A second look," Argonne National Lab Report, 1998.

[10] I. D. Hassan, R. M. Bucci, and K. T. Swe, "400 MW SMES power conditioning system development and simulation," *Trans. Power Electron.*, vol. 8, pp. 237–249, Jul. 1993.

[11] Q. Jiang and M. F. Conlon, "The power regulation of a PWM type superconducting magnetic energy storage unit," *IEEE Trans. Energy Convers.*, vol. 11, no. 1, pp. 168–174, Mar. 1996.

[12] W. R. Lachs and D. Sutanto, "Battery storage plant within large load centers," *IEEE Trans. Power Syst.*, vol. 7, no. 2, pp. 762–769, May 1992.

[13] M. A. Casacca, M. R. Capobianco, and Z. M. Salameh, "Lead-acid battery storage configurations for improved available capacity," *IEEE Trans. Energy Convers.*, vol. 11, no. 1, pp. 139–145, Mar. 1996.

[14] N. W. Miller *et al.*, "Design and commissioning of a 5 MVA, 2.5 MWh battery energy storage," in *Proc. IEEE Power Eng. Soc. Transm. Distrib. Conf.*, 1996, pp. 339–345.

[15] N. Abi-Samra, C. Neft, A. Sundaram, and W. Malcolm, "The distribution system dynamic voltage restorer and its applications at industrial facilities with sensitive loads," in *Proc. 8th Int. Power Qual. Solutions*, Long Beach, CA, USA, Sep. 9–15, 1995.

[16] L. Xiangjun, H. Dong, and L. Xiaokang, "Battery energy storage station (BESS)-based smoothing control of photovoltaic (PV) and wind power generation fluctuations," *IEEE Trans. Sustain. Energy*, vol. 4, no. 2, pp. 464–473, Apr. 2013.

[17] M. J. E. Alam, K. M. Muttaqi, and D. Sutanto, "A novel approach for ramp-rate control of solar PV using energy storage to mitigate output fluctuations caused by cloud passing," *IEEE Trans. Energy Convers.*, vol. 29, no. 2, pp. 507–518, Apr. 2013.

[18] S. A. Abdelrazek, S. Kamalasadan, and J. Enslin, "An approach for control of battery energy storage management systems considering multiple functions," in *Proc. IEEE PES Gener. Meeting*, Jul. 27–31, 2014, pp. 1–5.

[19] S. Abdelrazek and S. Kamalasadan, "Integrated control of battery energy storage management system considering PV capacity firming and energy time shift applications," in *Proc. IEEE Ind. Appl. Soc. Annu. Meeting*, Oct. 5–9, 2014, pp. 1–7.

[20] S. Abdelrazek and S. Kamalasadan, "A novel integrated optimal battery energy management control architecture considering multiple storage functions," in *Proc. North Amer. Power Symp. (NAPS)*, Sep. 7–9, 2014, pp. 1–6.

[21] S. G. Tesfahunegn, Ø. Ulleberg, P. J. Vie, and T. M. Undeland, "PV fluctuation balancing using hydrogen storage–A smoothing method for integration of PV generation into the utility grid," *Energy Procedia*, vol. 12, pp. 1015–1022, 2011.

[22] O. Tremblay and L. Dessaint, "Experimental validation of a battery dynamic model for EV applications," *World Elect. Veh. J.*, vol. 3, pp. 1–10, 2009.

[23] D. Sowder, "Mitigating solar intermittency using energy storage on a utility distribution system," in *Proc. IEEE Clemson Univ. Power Syst. Conf. Expo.*, Feb. 13, 2013.

Sherif A. Abdelrazek (S'12) was born in Cairo, Egypt, in 1988. He received the B.S. degree in electrical power and machines engineering from Ain Shams University, Cairo, Egypt, in 2010, and the M.S. and Ph.D. degrees in electrical engineering from the University of North Carolina at Charlotte, Charlotte, NC, USA, in 2015.

From 2012 to 2015, he was a Research Assistant with the Power, Energy, and Intelligent Systems Laboratory (PEISL), Energy Production and Infrastructure Center (EPIC), Charlotte, NC, USA. He is currently an Engineer with Duke Energy, Charlotte, NC, USA. He holds two patents. His research interests include energy storage systems applications, distribution systems stability, power electronics, distributed generation, PV stations design optimization, microgrid design, and distribution-level renewables penetration enhancement.

Dr. Abdelrazek was the recipient of the Egyptian Syndicate of Engineer's Award in 2007, the Degree of Honor from Ain Shams University in 2010, and the Siemens Masters of Energy Scholarship in 2015.

Sukumar Kamalasadan (M'04) received the B.Tech. degree in electrical engineering from the University of Calicut, India, in 1991, the M.Eng. degree in electric power system management from the Asian Institute of Technology, Bangkok, Thailand, in 1999, and the Ph.D. degree in electrical engineering from the University of Toledo, Toledo, OH, USA, in 2004.

He is an Associate Professor with the Department of Electrical and Computer Engineering and an Associate of the Energy Production and Infrastructure Center, University of North Carolina at Charlotte, Charlotte, NC, USA. He has over 22 years of combined academic and industry experience. He has authored/coauthored over 100 technical journal and conference papers for the IEEE and other organizations, and has written five chapters in scientific books and authored one book. His research interests include smart grid, microgrid, power system operation and optimization, power system dynamics, stability, and control, and renewable-energy-based distributed generation.

Dr. Kamalasadan is involved in several committees with the IEEE and was the General Co-Chair of the 2015 North American Power Symposium. He was the recipient of several awards including the National Science Foundation Faculty Early CAREER Award in 2008 and the Best Paper Award from the IEEE in 2015.